crystals

MDPI

Article

Relation between Electronic Structure and Thermoelectric Properties of Heusler-Type Ru_2VAl Compounds

Hidetoshi Miyazaki [1,2,*], Shin-ichi Kimura [3,4], Kensuke Onishi [2], Takehiko Hihara [1,2], Masato Yoshimura [5], Hirofumi Ishii [5], Masashi Mikami [6] and Yoichi Nishino [1]

1 Department of Physical Science and Engineering, Nagoya Institute of Technology, Nagoya 466-8555, Japan
2 Creative Engineering Program, Nagoya Institute of Technology, Nagoya 466-8555, Japan
3 FBS and Department of Physics, Osaka University, Suita 565-0871, Japan
4 Institute for Molecular Science, Okazaki 444-8585, Japan
5 National Synchrotron Radiation Research Center, Hsinchu 30076, Taiwan
6 National Institute of Advanced Industrial Science and Technology, Nagoya 463-8560, Japan
* Correspondence: miyazaki@nitech.ac.jp; Tel.: +81-52-735-5394

Abstract: We investigated Heusler-type Ru_2VAl, a candidate material for next-generation thermoelectric conversion, by first-principle calculations of its thermoelectric conversion properties and direct experimental observations of its electronic structures, employing photoemission and infrared spectroscopy. Our results show that Ru_2VAl has a wider pseudogap near the Fermi level compared to Fe_2VAl. Accordingly, a higher thermoelectric conversion performance can be expected in Ru_2VAl at higher temperatures.

Keywords: Heusler-type Ru_2VAl; first-principle calculation; photoemission spectroscopy; infra-red spectroscopy; thermoelectric properties; electronic structure

check for updates

Citation: Miyazaki, H.; Kimura, S.-i.; Onishi, K.; Hihara, T.; Yoshimura, M.; Ishii, H.; Mikami, M.; Nishino, Y. Relation between Electronic Structure and Thermoelectric Properties of Heusler-Type Ru_2VAl Compounds. *Crystals* **2022**, *12*, 1403. https://doi.org/10.3390/cryst12101403

Academic Editors: Wei Ren and Zhilun Lu

Received: 5 September 2022
Accepted: 28 September 2022
Published: 4 October 2022

Publisher's Note: MDPI stays neutral with regard to jurisdictional claims in published maps and institutional affiliations.

Copyright: © 2022 by the authors. Licensee MDPI, Basel, Switzerland. This article is an open access article distributed under the terms and conditions of the Creative Commons Attribution (CC BY) license (https://creativecommons.org/licenses/by/4.0/).

1. Introduction

Thermoelectric conversion has attracted considerable attention in recent years as the next generation of green energy because it can convert thermal energy into electrical energy. The performance of thermoelectric materials is evaluated using the power factor, P, and the non-dimensional figure of merit ZT, which are expressed by the following equations:

$$P = \frac{S^2}{\rho},$$

$$ZT = \frac{S^2}{\rho\,\kappa}T,$$

where S is the Seebeck coefficient, ρ is the electrical resistivity, and κ is the thermal conductivity. Bi_2Te_3 [1–3], PbTe [4], and SiGe [5–7] are typical thermoelectric materials used in practical applications. Bi_2Te_3, in particular, is used in thermoelectric power generation and laser diode cooling units, and its ZT is approximately 1.2 to 1.4 [8–11]. However, the performance of these materials has not significantly improved in recent years, and the development of new thermoelectric materials is desired.

Recently, Nishino suggested that material systems with valley-like electronic structures near the Fermi level E_F, such as pseudogap-like electronic structures, are promising for thermoelectric conversion [12,13]. Based on Mott's theory [14], the Seebeck coefficient of a typical metal can be expressed as follows:

$$S = -\frac{\pi^2}{3}\frac{k_B^2 T}{e}\left[\frac{1}{N(E)}\frac{\partial N(E)}{\partial E}\right]_{E=E_F},$$

where e is the electron charge, $N(E)$ is the density of states (DOS), and k_B is Boltzmann's constant. According to this equation, the Seebeck coefficient is inversely proportional to the absolute value of the DOS at E_F and proportional to its energy gradient. Therefore, by adjusting E_F to the appropriate DOS position through carrier doping by elemental substitution, high Seebeck coefficients can be expected for both *p*- and *n*-type materials. In fact, it has been shown that high thermoelectric performance can be achieved by controlling the position of E_F in the pseudogap in Heusler-type Fe_2VAl with an ideal pseudogap-like electronic structure [15–24].

For the electron-doped Heusler-type $Fe_2VAl_{1-x}Si_x$ compound [15], $P = 5.4 \times 10^{-3}$ W/mK^2, is larger than the power factor of *n*-type Bi_2Te_3 material. In contrast, $P = 2.3 \times 10^{-3}$ W/mK^2 for hole-doped $Fe_2V_{1-x}Ti_xAl$ [16]. However, the shortcomings of the Heusler compounds are that their high power factor ranges from room temperature to 400 K and their performance is low in the mid-temperature range of 400 to 600 K. In addition, cubic Heusler-type crystal structures have a high crystal symmetry, resulting in a thermal conductivity of approximately 25 W/mK^2, [25] which is approximately 10 times higher than that of Bi_2Te_3. To further improve the thermoelectric performance, it is necessary to search for materials that form pseudogap-like electronic structures even with low thermal conductivity.

One way to reduce thermal conductivity without significantly changing the electronic structure is to replace some of the constituent elements with heavier elements. First-principle calculations have shown that when Fe is replaced by Ru (same group as Fe but with a larger atomic number), as in Ru_2VAl, a wider pseudogap is formed in E_F compared to Fe_2VAl [26,27]. In addition, Ru_2VAl, synthesized by Ramachandran et al., has a thermal conductivity of 10 W/mK^2, which is approximately 40% lower than that of Fe_2VAl [28]. Thus, Heusler-type Ru_2VAl is a candidate for next-generation thermoelectric conversion materials, surpassing the thermoelectric performance of Fe_2VAl.

For Fe_2VAl, the relationship between the electronic structure and thermoelectric conversion properties by photoelectron spectroscopy [29–36] and infrared (IR) spectroscopy [37,38] has been discussed in detail. The pseudogap width in Fe2VAl is actually much smaller than predicted by band calculations due to the strong electron correlation induced by the Fe atoms [39]. Based on the understanding of this difference in electronic structure, significant performance improvements have been achieved based on the material design utilizing the electronic structure of Fe_2VAl. Therefore, knowledge of the electronic structure is essential for improving the performance of thermoelectric conversion materials. However, for Ru_2VAl, only band-structure calculations are available and there are no experimental observations. Therefore, in this work, we discuss the potential of Ru_2VAl as a thermoelectric conversion material by attempting to relate the electronic structure and thermoelectric conversion properties using first-principle calculations and experimental observations.

2. Theoretical and Experimental Methods

The electronic band structures of Fe_2VAl and Ru_2VAl were calculated using the full-potential linearized augmented plane-wave method and generalized gradient approximation as implemented in the WIEN2k package [39]. The equilibrium crystal structure was determined by minimizing the total energy, which was achieved by relaxing the lattice parameters. The convergence energy threshold was set to 0.0001 Ry. The theoretical thermoelectric properties were calculated using the Boltzmann transport equation within the constant relaxation time approximation using the BoltzTraP code based on the WIEN2k electronic structure [40].

Ingots of Fe_2VAl and Ru_2VAl alloys were prepared by repeated arc melting of appropriate mixtures of 99.99% pure Fe, Ru and Al, and 99.9% pure V in an argon atmosphere. For hard X-ray photoemission spectroscopy (HAXPES) and IR measurements, 1 mm × 1 mm × 3 mm and 3 mm × 3 mm × 2 mm samples were used. Each sample was cut from a disk with a SiC blade, sealed in an evacuated quartz capsule, and annealed at 1273 K for 1 h and then at 673 K for 4 h, followed by furnace cooling.

High-resolution synchrotron radiation X-ray powder diffraction (SR-XRD) measurements were performed at 300 K using the BL02B2 beamline (wavelength = 0.04600 nm), SPring-8 [41]. The wavelength was precisely calibrated using a CeO_2 standard sample. The VESTA program was used to simulate XRD patterns [42].

HAXPES measurements were performed at BL12XU of the SPring-8 Taiwan beamlines, and all photoemission spectra were recorded at room temperature. A clean surface of the material for HAXPES measurement was obtained by ex situ fracturing with a knife edge and immediately installing the sample in the HAXPES chamber. E_F and total energy resolution were determined from the Fermi edge of the gold films. The total energy resolution of the HAXPES measurements was set to 310 meV at an excitation photon energy ($h\nu$) of 6916 eV.

IR measurements were performed using a Fourier interferometer (FTIR6100, JASCO Inc.) in the temperature range of 10–300 K. The surface of the sample was then polished to a mirror finish. The absolute value of reflectivity was determined by dividing the measured data from the calibration spectrum obtained by depositing gold on the sample surface after IR spectroscopy measurement of the sample.

3. Results and Discussions

Figure 1a,b show the volume dependence of the total energies of Fe_2VAl and Ru_2VAl, respectively. As shown in Table 1, the lattice parameters and Young's moduli were derived by fitting the obtained volume dependence of the total energy to the Birch–Murnaghan equation of state. Experimental lattice constants were calculated from XRD measurements on the fabricated materials. The calculated lattice parameters and Young's moduli were in good agreement with previously reported calculations for both Fe_2VAl [43,44] and Ru_2VAl [26,27]. Comparing the experimental and calculated lattice parameters obtained from SR-XRD measurements, which will be discussed in the next session, the experimental lattice parameter is larger for Fe_2VAl but comparable for Ru_2VAl. In general, the lattice parameter calculated by the GGA method tends to be slightly larger than the experimental value. The discrepancy in the trend of the difference between the experimental and calculated lattice parameters of Ru_2VAl is discussed in the next section. The calculated Young's modulus is larger for Ru_2VAl than for Fe_2VAl, indicating a higher strength. This is expected to increase the overall strength of the module and improve its reliability when a thermoelectric conversion module is fabricated using Ru_2VAl.

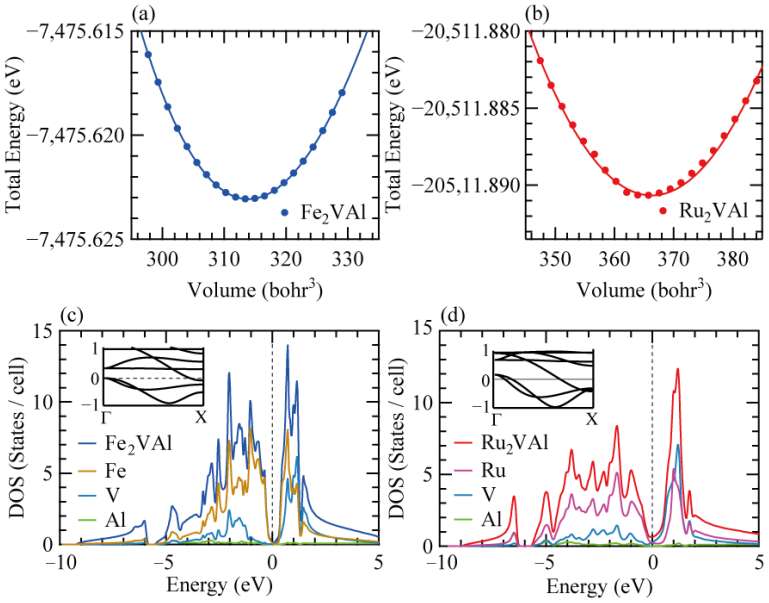

Figure 1. Volume dependence of the total energy of Fe_2VAl (**a**) and Ru_2VAl (**b**). The curves are the result of fitting with the Birch–Murnaghan equation of state. Calculated density of states of Fe_2VAl (**c**) and Ru_2VAl (**d**). The inset shows the band structure along the Γ–X line.

Table 1. Lattice parameter and Young's modulus of Fe_2VAl and Ru_2VAl.

	Fe_2VAl	**Ru_2VAl**
Lattice parameter (nm)	0.5709	0.6011
Experimental Lattice parameter (nm)	0.5761	0.5994
Young module (GPa)	223.05	256.03

Figure 1c,d show the DOS of Fe_2VAl and Ru_2VAl, respectively. Both the DOSs exhibit a pseudogap-like feature with a sharp drop in DOS close to E_F. The magnitude of the DOS at E_F was similar for Fe_2VAl and Ru_2VAl. In Fe_2VAl, the sizes of the hole and electron pockets were almost the same, whereas, in Ru_2VAl, the hole pocket was larger than the electron pocket. As a result, the pseudogap structure of Ru_2VAl is asymmetric between the valence and conduction band sides, with a gradual increase on the conduction band side, resulting in a wider pseudogap than that of Fe_2VAl. Because of this larger pseudogap width in Ru_2VAl compared to Fe_2VAl, the peak temperature of the absolute Seebeck coefficient is expected to shift to a higher temperature. This shift is caused by the thermal excitation of carriers that are suppressed in Ru_2VAl compared to Fe_2VAl at high temperatures. To discuss the effect of the difference in DOS between Fe_2VAl and Ru_2VAl on the Seebeck coefficient and power factor, we next discuss the electronic transport properties calculated from the obtained electronic structures using the Boltzmann transport equation.

Figure 2a,b show the chemical potential dependence of the Seebeck coefficients for Fe_2VAl and Ru_2VAl calculated in the range 300–1000 K. Fe_2VAl shows a maximum positive value of 140 μV/K, a maximum negative value of −110 μV/ K, and large Seebeck coefficients for both p- and n-type materials. In contrast, Ru_2VAl has a large Seebeck coefficient for p-type materials with a maximum positive value of 70 μV/K but a small Seebeck coefficient value of −30 μV/K for n-type materials. Figure 2c,d show the chemical potential dependence of the calculated power factors for Fe_2VAl and Ru_2VAl in the 300–1000 K range. The power factor of the calculation is not directly comparable to the power factor of the experiment because the units are different from those of the experiment, since the relaxation time cannot be calculated in the band calculation. The Seebeck coefficient is generally smaller for Ru_2VAl than for Fe_2VAl, but the power factor is similar for both p-type materials with 125×10^{10} W/K^2 cm s at 1000 K. The smaller *n*-type thermoelectric properties can be attributed to the larger hole pocket in Figure 1d. In other words, when the material is electron-doped, E_F shifts to the conduction band side, but the large hole pocket reduces the slope of the DOS at E_F, resulting in a smaller Seebeck coefficient and thus a smaller power factor in Ru_2VAl.

Figure 3 shows the SR-XRD measurements on Fe_2VAl and Ru_2VAl. The overall X-ray diffraction patterns of Fe_2VAl and Ru_2VAl were identified as a single-phase Heusler-type ($L2_1$) structure. However, the diffraction peak due to the (111) mirror plane, which should be observed around 7°, was not observed for Ru_2VAl. This result, together with the fact that the experimental and calculated lattice parameter are comparable, suggests that Ru_2VAl may not be completely ordered $L2_1$ structure, but may have a partially disordered $B2$ structure. In order to obtain the $L2_1$ ordered phase of Ru_2VAl in the future, it is necessary to explore for the optimum heat treatment conditions for ordering.

Next, we discuss the agreement of the calculated DOS with the experimentally observed DOS. Figure 4a shows a wide range of core–electron photoemission spectra of Fe_2VAl and Ru_2VAl for each core–electron state of the constituent elements in Fe_2VAl and Ru_2VAl. The observed photoelectron spectra can be entirely attributed to the core–electron states of the constituent elements, and oxygen and carbon adsorbed on the surface before the sample was introduced into the HAXPES chamber. The core–electron states of Al 1*s* (b), V $2p_{3/2}$ (c), Fe $2p_{3/2}$ (d), and Ru $3d_{5/2}$ (e) in Fe_2VAl and Ru_2VAl are shown in Figure 4. Two peaks are observed near 1558 eV and 1562 eV for the Al 1*s* state. The broad peak observed at the high-binding-energy side is attributed to Al_2O_3 associated with surface oxidation [45]. In contrast, no oxidation-induced peak structures are visible for the

other constituent elements Ru, Fe, and V. In general, Al_2O_3 is a stable surface oxide film, and when an Al_2O_3 surface-oxide film is formed, oxygen is less likely to diffuse into the interior at high temperatures, improving the oxidation resistance [46]. Therefore, Ru_2VAl, like Fe_2VAl, is expected to have high thermal stability at high temperatures and can be adapted to thermoelectric conversion modules that are stable at high temperatures. The peak positions of Al 1*s* and V $2p_{3/2}$ shift towards higher binding energies in Ru_2VAl than in Fe_2VAl. As shown in Figure 4b,c, the trend of this shift is consistent with the energy difference of the core–electron states expected from the all-electron calculations shown in Figure 1. The probability of the existence of the wave function in the Ru 4*d* state is more spatially extended than that in the Fe 3*d* state. Therefore, the DOS near E_F in Ru_2VAl is expected to be strongly hybridized than that in Fe_2VAl, resulting in a wider pseudo-gap. Therefore, the peaks of the Al and V core electron states in Ru_2VAl with stronger hybridization are located on the higher binding energy side compared to Fe_2VAl, and this interpretation is consistent with the experimental and calculated results.

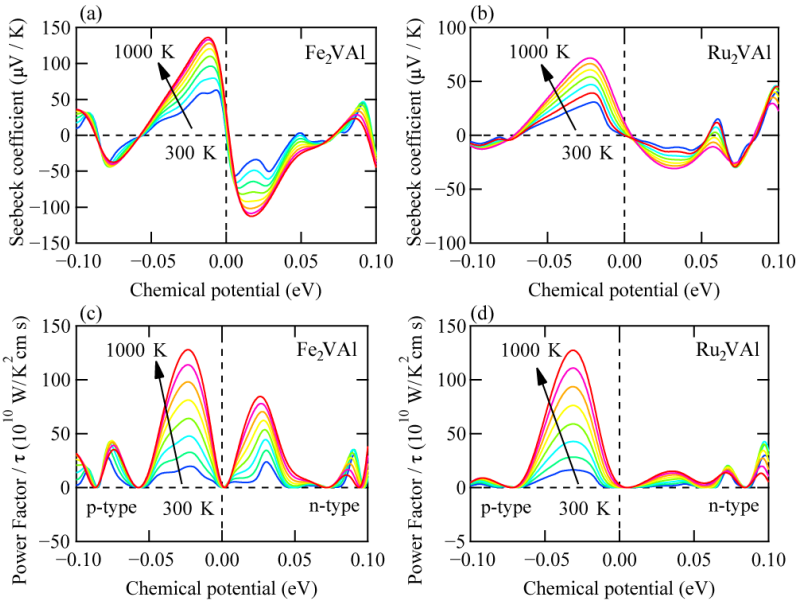

Figure 2. Chemical potential dependence of Seebeck coefficients and power factor for Fe_2VAl (**a**,**c**) and Ru_2VAl (**b**,**d**) calculated in the range of 300–1000 K.

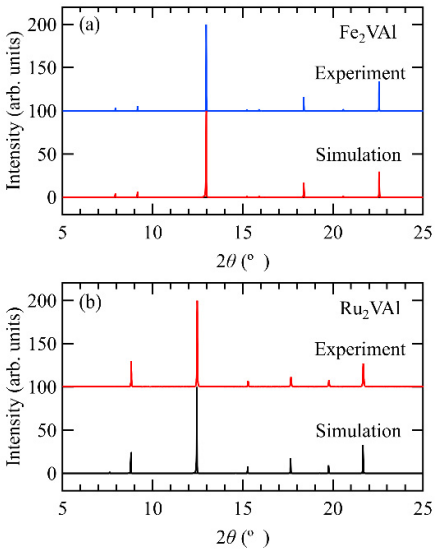

Figure 3. Powder X-ray diffraction patterns for Fe_2VAl (**a**) and Ru_2VAl (**b**).

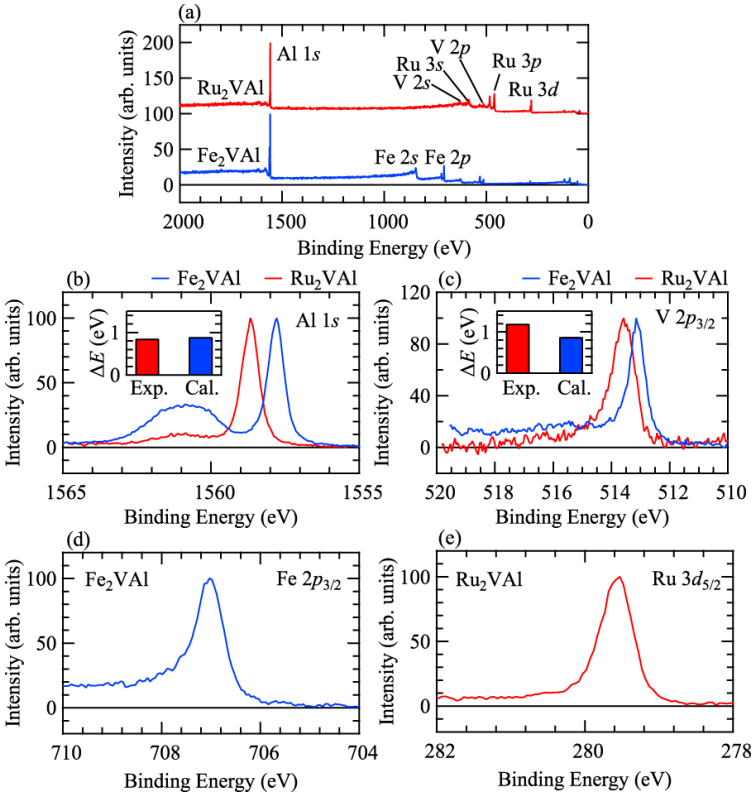

Figure 4. Wide photoemission spectra (**a**) and core level photoemission spectra of Al 1*s* (**b**), V $2p_{3/2}$ (**c**), Fe $2p_{3/2}$ (**d**) and Ru $3d_{3/2}$ (**e**) states Fe_2VAl and Ru_2VAl.

Figure 5a,b show the experimental and calculated valence band photoemission spectra of Ru_2VAl and Fe_2VAl. The calculated valence band photoelectron spectra were obtained by considering the photoexcitation cross-sections [47] at the excitation photon energies used for the HAXPES measurements for each constituent element in DOS in Figure 1c,d. The SR-XRD results suggest that Ru_2VAl may not be a completely ordered-$L2_1$ structure, but the effect of the disordered-*B*2 structure on the electronic structure is considered to be very small because no broadening of the photoelectron spectrum was observed when comparing the photoelectron spectra of Ru_2VAl and Fe_2VAl. The photoelectron spectrum of Ru_2VAl shows a large peak around 1.5 eV, which is not observed in Fe_2VAl. This state is emphasized because the photoexcitation cross-section of Ru 4*d* state is larger than that of the Fe 3*d* state. Similar to Fe_2VAl, Ru_2VAl has a pseudogap electronic structure with low photoelectron intensity near the E_F. The increase in the intensity of the photoelectron spectrum from the E_F in Ru_2VAl is comparable to that in Fe_2VAl. This result is in agreement with the band calculation results, where the DOS on the valence band side is similar for both, and the difference in the pseudogap width is attributed to the different density of states on the conduction band side.

Photoelectron spectroscopy measurements can only reveal the electronic structure of the valence band and not the conduction band. Infrared spectroscopy allows us to observe the reflectivity representing the electronic structure of both the valence and conduction bands. Therefore, IR is a useful tool in elucidating the details of the electronic structure near E_F. Figure 6 shows the photon energy dependence of the reflectivity of Ru_2VAl. Overall reflectivity showed a gradual decrease with increasing photon energy, reflecting the semi-metallic electronic structure. The overall shape of the temperature dependence of reflectivity remained unaltered, but the reflectivity gradually decreased with increasing measurement temperature. This result suggests a decrease in the number of carriers with decreasing measurement temperatures. This result is qualitatively consistent with the electronic resistivity measurement results, which show an increase in the electrical resistivity with

increasing temperature. The reflectivity changes abruptly at about 0.03 eV and 0.2 eV, with the latter change in reflectivity energy being related to the width of the pseudogap based on previous IR results for Fe_2VAl [39]. This suggests that Ru_2VAl has a larger pseudogap than Fe_2VAl, which is consistent with the band calculations. However, we did not observe an abrupt phenomenon in the DOS below 0.02 eV, as observed in the IR measurements of Fe_2VAl. This may be due to the strong electronic correlation of Fe 3*d* in Fe_2VAl; such a decrease in reflectivity was not observed in Ru_2VAl, which has a stronger itinerant nature, as observed in SrM_4Sb_{12} (*M* = Fe, Ru) [48]. The pseudogap width of Ru_2VAl is expected to be similar to the band calculation result due to the itinerant nature of Ru atoms. Therefore, Ru_2VAl is expected to have a higher Seebeck coefficient peak at higher temperatures than Fe_2VAl due to its wider pseudogap width, and is expected to be a thermoelectric conversion material with higher performance at higher temperatures than Fe_2VAl.

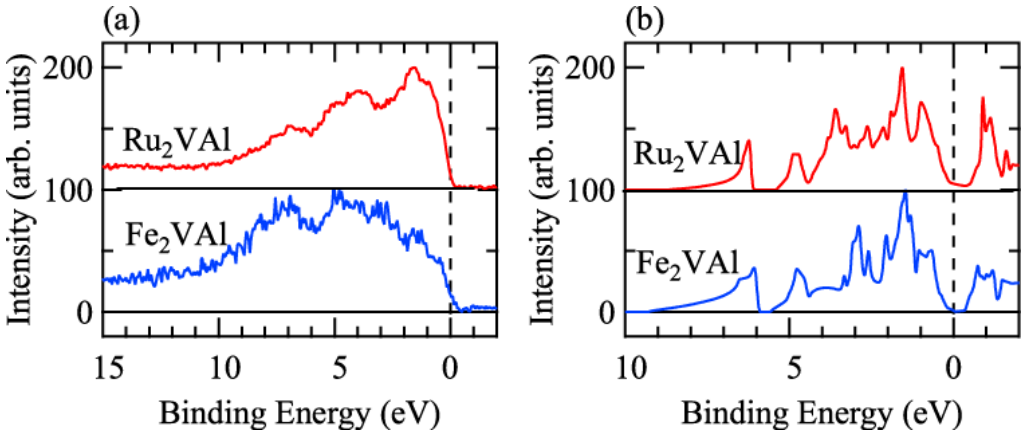

Figure 5. Experimental (**a**) and simulated (**b**) photoemission spectra of Fe_2VAl and Ru_2VAl with $h\nu$= 6916 eV.

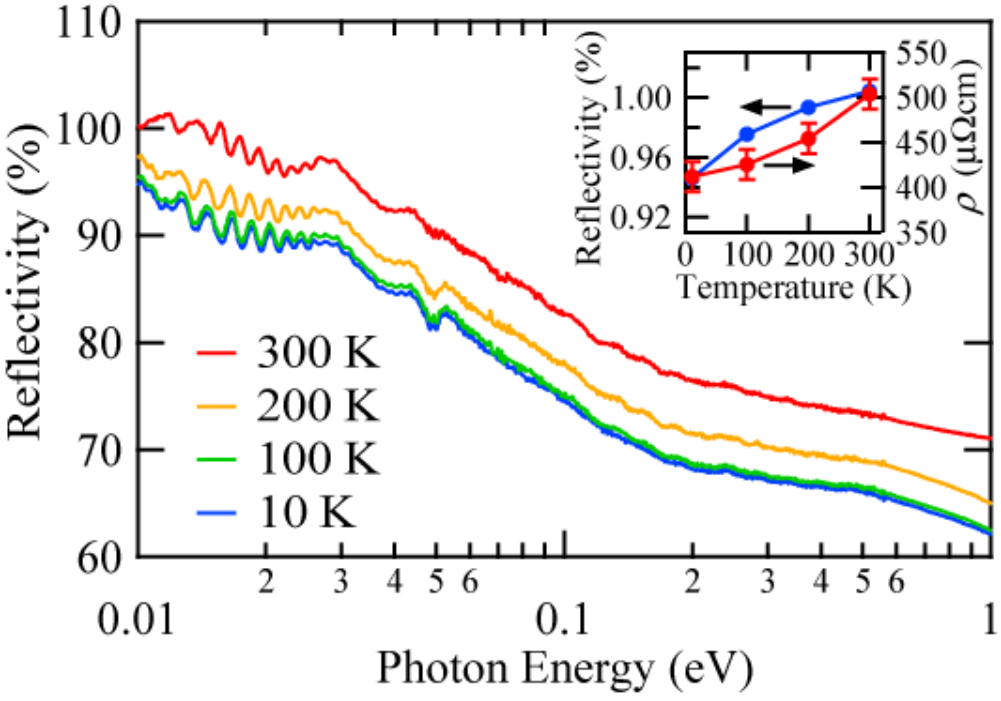

Figure 6. Photon energy dependence of reflectivity in Ru_2VAl.

4. Conclusions

In this study, first-principle calculations of the thermoelectric conversion properties and direct observation of the electronic structure by photoelectron and infrared spectroscopy were performed to investigate the potential of Heusler-type Ru_2VAl alloys as thermoelectric materials. First-principle calculations showed that the *n*-type power factor is smaller in Ru_2VAl than in Fe_2VAl, but the *p*-type power factor is comparable. Compared with Fe_2VAl, Ru_2VAl has a lower thermal conductivity owing to its higher density. Therefore, *ZT*, which is a performance index that includes the thermal conductivity, is expected to be large. A comparison of the electronic structures of Ru_2VAl and Fe_2VAl shows that Ru_2VAl has a wider pseudogap, which was confirmed experimentally and theoretically. This result may be due to the shift of the peak temperature of the thermoelectric conversion property to the higher-temperature side of Ru_2VAl. Based on these results, Ru_2VAl is expected to be a candidate material for next-generation thermoelectric conversion materials with better thermoelectric conversion properties at higher temperatures compared to Fe_2VAl.

Author Contributions: H.M. performed the theoretical band structure calculations. H.M., M.Y. and H.I. performed HAXPES experiments. H.M., K.O. and S.-i.K. performed the IR spectroscopy experiments. H.M. and S.-i.K. were responsible for data analysis and writing of the paper. T.H., M.M. and Y.N. reviewed and editing of the paper. Y.N. supervised this project. All the authors discussed the results and commented on the manuscript. All authors have read and agreed to the published version of the manuscript.

Funding: This study was partly supported by a JSPS KAKENHI Grant-in-Aid for Scientific Research (C) (Nos. 18K04748 and 20K05060). This project was supported by the public interest of the Tatematsu and Hibi Science Foundation.

Institutional Review Board Statement: Not applicable.

Informed Consent Statement: Not applicable.

Data Availability Statement: Not applicable.

Acknowledgments: HAXPES measurements were performed at the SPring-8 synchrotron facility with approval from the Taiwan beamline. SR-XRD measurements were performed at the SPring-8 synchrotron facility with approval of JASRI (Proposal No. 2021A1462). The computations were supported by Research Center for Computational Science, Okazaki, Japan (Project: 21-IMS-C093) and by the Advanced Research Infrastructure for Materials and Nanotechnology (ARIM) program in Japan. We would like to thank.

Conflicts of Interest: The authors declare no conflict of interest.

References

1. Amin Bhuiyan, M.R.; Mamur, H.; Dilmaç, Ö.F. A Review on Performance Evaluation of Bi2Te3-based and some other Thermoelectric Nanostructured Materials. *Curr. Nanosci.* **2021**, *17*, 423–446. [CrossRef]
2. Chen, Y.; Hou, X.; Ma, C.; Dou, Y.; Wu, W. Review of Development Status of Bi_2Te_3-Based Semiconductor Thermoelectric Power Generation. *Adv. Mater. Sci. Eng.* **2018**, *2018*, 1210562. [CrossRef]
3. Mamur, H.; Bhuiyan, M.R.A.; Korkmaz, F.; Nil, M. A review on bismuth telluride (Bi_2Te_3) nanostructure for thermoelectric applications. *Renew. Sust. Energ. Rev.* **2018**, *82*, 4159. [CrossRef]
4. Su, C.-H. Design, growth and characterization of PbTe-based thermoelectric materials. *Prog. Cryst. Growth Charact. Mater.* **2019**, *65*, 47–94. [CrossRef]
5. Nozariasbmarz, A.; Agarwal, A.; Coutant, Z.A.; Hall, M.J.; Liu, J.; Liu, R.; Malhotra, A.; Norouzzadeh, P.; Öztürk, M.C.; Ramesh, V.P.; et al. Thermoelectric silicides: A review. *Jpn. J. Appl. Phys.* **2017**, *56*, 05DA04. [CrossRef]
6. Basu, R.; Singh, A. High temperature Si–Ge alloy towards thermoelectric applications: A comprehensive review. *Mater. Today Phys.* **2021**, *21*, 100468. [CrossRef]
7. Li, Y.; Wang, G.; Akbari-Saatlu, M.; Procek, M.; Radamson, H.H. Si and SiGe Nanowire for Micro-Thermoelectric Generator: A Review of the Current State of the Art. *Front. Mater.* **2021**, *8*, 611078. [CrossRef]
8. Chen, Z.; lin, M.Y.; Xu, G.D.; Chen, S.; Zhang, J.H.; Wang, M.M. Hydrothermal synthesized nanostructure Bi–Sb–Te thermoelectric materials. *J. Alloys Compd.* **2014**, *588*, 384–387. [CrossRef]
9. Tan, M.; Deng, Y.; Hao, Y. Enhancement of thermoelectric properties induced by oriented nanolayer in $Bi_2Te_{2.7}Se_{0.3}$ columnar films. *Mater. Chem. Phys.* **2014**, *146*, 153–158. [CrossRef]

10. Tan, M.; Hao, Y.; Wang, G. Improvement of thermoelectric properties induced by uniquely ordered lattice field in $Bi_2Se_{0.5}Te_{2.5}$ pillar array. *J. Solid State Chem.* **2014**, *215*, 219–224. [CrossRef]
11. Ahmad, K.; Wan, C. Enhanced thermoelectric performance of Bi2Te3 through uniform dispersion of single wall carbon nanotubes. *Nanotechnology* **2017**, *28*, 415402. [CrossRef] [PubMed]
12. Nishino, Y.; Kato, M.; Asano, S.; Soda, K.; Hayasaki, M.; Mizutani, U. Semiconductorlike Behavior of Electrical Resistivity in Heusler-type Fe_2VAl Compound. *Phys. Rev. Lett.* **1997**, *79*, 1909. [CrossRef]
13. Nishino, Y. *The Science of Complex Alloy Phases*; TMS: Warrendale, PA, USA, 2005; pp. 325–344.
14. Mott, N.F.; Jones, H. *The Theory of the Properties of Metals*; Clarendon Press: Oxford, UK, 1936.
15. Kato, H.; Kato, M.; Nishino, Y.; Mizutani, U.; Asano, S. Effect of Silicon Substitution on Thermoelectric Properties of Heusler-type Fe_2VAl Alloy. *J Jpn. Inst. Metal.* **2001**, *65*, 652. [CrossRef]
16. Matsuura, H.; Nishino, Y.; Mizutani, U.; Asano, S. Doping Effects on Thermoelectric Properties of the Pseudogap Fe_2VAl System. *J Jpn. Inst. Metal.* **2002**, *66*, 767. [CrossRef]
17. Lue, C.S.; Chen, C.F.; Lin, J.Y.; Yu, Y.T.; Kuo, Y.K. Thermoelectric properties of quaternary Heusler alloys $Fe_2VAl_{1-x}Si_x$. *Phys. Rev. B* **2007**, *75*, 064204. [CrossRef]
18. Vasundhara, M.; Srinivas, V.; Rao, V.V. Electronic transport in Heusler-type $Fe_2VAl_{1-x}M_x$ alloys (M = B,In,Si). *Phys. Rev. B* **2008**, *77*, 224415. [CrossRef]
19. Mikami, M.; Tanaka, S.; Kobayashi, K. Thermoelectric properties of Sb-doped Heusler Fe_2VAl alloy. *J. Alloys Compd.* **2009**, *484*, 444. [CrossRef]
20. Terazawa, Y.; Mikami, M.; Itoh, T.; Takeuchi, T. Effects of Heavy Element Substitution on Electronic Structure and Lattice Thermal Conductivity of Fe_2VAl Thermoelectric Material. *J. Electron. Mater.* **2012**, *41*, 1348. [CrossRef]
21. Miyazaki, H.; Renard, K.; Inukai, M.; Soda, K.; Nishino, Y. Electronic structure of Heusler-type $Fe_2V_{1+x}Al_{1-x}$ thermoelectric materials. *J. Electron Spectros. Relat. Rhenomena* **2014**, *195*, 185–188. [CrossRef]
22. Nishino, Y.; Tamada, Y. Doping effects on thermoelectric properties of the off-stoichiometric Heusler compounds $Fe_{2-x}V_{1+x}Al$. *J. Appl. Phys.* **2014**, *115*, 123707. [CrossRef]
23. Renard, K.; Mori, A.; Yamada, Y.; Tanaka, S.; Miyazaki, H.; Nishino, Y. Thermoelectric properties of the Heusler-type $Fe_2VTa_xAl_{1-x}$ alloys. *J. Appl. Phys.* **2014**, *115*, 033707. [CrossRef]
24. Nishino, Y.; Kamizono, S.; Miyazaki, H.; Kimura, K. Effects of off-stoichiometry and Ti doping on thermoelectric performance of Fe_2VAl Heusler compound. *AIP Adv.* **2019**, *9*, 125003. [CrossRef]
25. Miyazaki, H.; Tanaka, S.; Ide, N.; Soda, K.; Nishino, Y. Thermoelectric properties of Heusler-type off-stoichiometric $Fe_2V_{1+x}Al_{1-x}$ alloys. *Mater. Res. Express* **2014**, *1*, 015901. [CrossRef]
26. Guezmir, A.; Rached, H.; Bentouaf, A.; Caid, M.; Benkhettou, N.; Rached, D.; Sidoumou, M. Theoretical insight of stabilities and optoelectronic features of Ru-based Heusler alloys: Ab-initio calculations. *Comput. Condens. Matter.* **2021**, *28*, e00573. [CrossRef]
27. Abbassa, H.; Hadjri-Mebarki, S.; Amrani, B.; Belaroussi, T.; Driss Khodja, K.; Aubert, P. Theoretical investigation of new Heusler alloys $Ru_2VGa_{1-x}Al_x$. *J. Alloys Compd.* **2015**, *637*, 557–563. [CrossRef]
28. Ramachandran, B.; Lin, Y.H.; Kuo, Y.K.; Kuo, C.N.; Gippius, A.A.; Lue, C.S. Thermoelectric properties of Heusler-type $Ru_2VAl_{1-x}Ga_x$ alloys. *Intermetallics* **2018**, *92*, 36–41. [CrossRef]
29. Soda, K.; Mizutani, T.; Yoshimoto, O.; Yagi, S.; Mizutani, U.; Sumi, H.; Nishino, Y.; Yamada, Y.; Yokoya, T.; Shin, A.; et al. High-resolution photoelectron spectroscopyof Heusler-type Fe_2VAl alloy. *J. Synchrotron Radiat.* **2002**, *9*, 233. [CrossRef]
30. Miyazaki, H.; Soda, K.; Yagi, S.; Kato, M.; Takeuchi, T.; Mizutani, U.; Nishino, Y. Surface and bulk electronic structures of Heusler-type Fe_2VAl. *J. Vac. Sci. Technol. A* **2006**, *24*, 1464. [CrossRef]
31. Miyazaki, H.; Soda, K.; Kato, M.; Yagi, S.; Takeuchi, T.; Nishino, Y. Soft X-ray photoemission study of the Heusler-type $Fe_2VAl_{1-z}Ge_z$ alloys. *J. Electron Spectros. Relat. Rhenomena* **2007**, *156-158*, 347. [CrossRef]
32. Soda, K.; Harada, S.; Kato, M.; Yagi, S.; Inukai, M.; Miyazaki, H.; Sandaiji, Y.; Tamada, Y.; Tanaka, S.; Sugiura, T.; et al. Soft X-ray photoemission study of thermoelectric alloys $Fe_{2-x-y}Ir_yV_{1+x}Al$ and $Fe_{2-x}V_{1+x-y}Ti_yAl$. *J. Electron Spectros. Relat. Rhenomena* **2011**, *184*, 236. [CrossRef]
33. Miyazaki, H.; Inukai, M.; Nishino, Y. Effect of Ta substitution on the electronic structure of Heusler-type Fe_2VAl-based alloy. *J. Appl. Phys.* **2016**, *120*, 125106. [CrossRef]
34. Miyazaki, H.; Tateishi, S.; Matsunami, M.; Soda, K.; Yamada, S.; Hamaya, K.; Nishino, Y. Direct observation of pseudo-gap electronic structure in the Heusler-type Fe_2VAl thin film. *J. Electron Spectros. Relat. Rhenomena* **2019**, *232*, 1–4. [CrossRef]
35. Asai, M.; Miyazaki, H.; Watanabe, K.; Yasui, A.; Takagi, Y.; Nishino, Y. Hard X-Ray Photoemission Study of Heusler-Type $Fe_{2-x}Re_xVAl$ Thermoelectric Compounds. *Phys. Stat. Sol. (b)* **2022**, *259*, 2100567. [CrossRef]
36. Soda, K.; Ikedo, W.; Hayashi, T.; Shirakawa, T.; Miyazaki, H.; Nishino, Y. Hard X-Ray Photoemission Study on Bulk Electronic Structure of Heusler-Type $Fe_{2-x}V_{1+x}Al$ Alloys. *J. Phys. Soc. Jpn.* **2022**, *91*, 064713. [CrossRef]
37. Okamura, H.; Kawahara, J.; Nanba, T.; Kimura, S.; Soda, K.; Mizutani, U.; Nishino, Y.; Kato, M.; Shimoyama, I.; Miura, H.; et al. Pseudogap Formation in the Intermetallic Compounds $(Fe_{1-x}V_x)_3Al$. *Phys. Rev. Lett.* **2000**, *84*, 3674. [CrossRef] [PubMed]
38. Feng, Y.; Rhee, J.Y.; Wiener, T.A.; Lynch, D.W.; Hubbard, B.E.; Sievers, A.J.; Schlagel, D.L.; Lograsso, T.A.; Miller, L.L. Physical properties of Heusler-like Fe_2VAl. *Phys. Rev. B* **2001**, *63*, 165109. [CrossRef]
39. Blaha, P.; Schwarz, K.; Tran, F.; Laskowski, R.; Madsen, G.K.H.; Marks, L.D. WIEN2k: An APW+lo program for calculating the properties of solids. *J. Chem. Phys.* **2020**, *152*, 074101. [CrossRef]

40. Madsen, G.K.H.; Singh, D.J. BoltzTraP. A code for calculating band-structure dependent quantities. *Comput. Phys. Commun.* **2006**, *175*, 67–71. [CrossRef]
41. Kawaguchi, S.; Takemoto, M.; Osaka, K.; Nishibori, E.; Moriyoshi, C.; Kubota, Y.; Kuroiwa, Y.; Sugimoto, K. High-throughput powder diffraction measurement system consisting of multiple MYTHEN detectors at beamline BL02B2 of SPring-8. *Rev. Sci. Instrum.* **2017**, *88*, 085111. [CrossRef]
42. Momma, K.; Izumi, F. VESTA 3 for three-dimensional visualization of crystal, volumetric and morphology data. *J. Appl. Crystallogr.* **2011**, *44*, 1272–1276. [CrossRef]
43. Xu, B.; Li, X.; Yu, G.; Zhang, J.; Ma, S.; Wang, Y.; Yi, L. The structural, elastic and thermoelectric properties of Fe_2VAl at pressures. *J. Alloys Compd.* **2013**, *565*, 22. [CrossRef]
44. Khalfa, M.; Khachai, H.; Chiker, F.; Baki, N.; Bougherara, K.; Yakoubi, A.; Murtaza, G.; Harmel, M.; Abu-Jafar, M.S.; Omran, S.B.; et al. Mechanical, electronic and thermodynamic properties of full Heusler compounds Fe_2VX(X = Al, Ga). *International J. Mod. Phys. B* **2015**, *29*, 1550229. [CrossRef]
45. Weiland, C.; Lysaght, P.; Price, J.; Huang, J.; Woicik, J.C. Hard x-ray photoelectron spectroscopy study of As and Ga out-diffusion in $In_{0.53}Ga_{0.47}As/Al_2O_3$ film systems. *Appl. Phys. Lett.* **2012**, *101*, 061602. [CrossRef]
46. Song, T.T.; Yang, M.; Chai, J.W.; Callsen, M.; Zhou, J.; Yang, T.; Zhang, Z.; Pan, J.S.; Chi, D.Z.; Feng, Y.P.; et al. The stability of aluminium oxide monolayer and its interface with two-dimensional materials. *Sci. Rep.* **2016**, *6*, 29221. [CrossRef]
47. Yeh, J.J.; Lindau, I. Atomic subshell photoionization cross sections and asymmetry parameters: $1 \leq Z \leq 103$. *At. Data Nucl. Data Tables* **1985**, *32*, 1. [CrossRef]
48. Kimura, S.-I.; Im, H.; Mizuno, T.; Narazu, S.; Matsuoka, E.; Takabatake, T. Infrared study on the electronic structure of the alkaline-earth-filled skutterudites AM_4Sb_{12} (A = Sr, Ba; M = Fe, Ru, Os). *Phys. Rev. B* **2007**, *75*, 245106. [CrossRef]